Controlling electron motion with attosecond precision by a shaped femtosecond intense laser pulse

Xiaoyun Zhao,[1,*] Mingqing Liu,[2,*] Yizhang Yang,[3] Zhou Chen,[3] Xiaolei Hao,[1,†] Chuncheng Wang,[3,‡] Weidong Li,[4] and Jing Chen[5,4,§]

[1]*Institute of Theoretical Physics and Department of Physics, State Key Laboratory of Quantum Optics and Quantum Optics Devices, Collaborative Innovation Center of Extreme Optics, Shanxi University, Taiyuan 030006, China*

[2]*School of Physics and Information Technology, Shaanxi Normal University, Xi'an 710119, China*

[3]*Institute of Atomic and Molecular Physics and Jilin Provincial Key Laboratory of Applied Atomic and Molecular Spectroscopy, Jilin University, Changchun 130012, China*

[4]*Shenzhen Key Laboratory of University Laser and Advanced Material Technology, Center for Advanced Material Diagnostic Technology, and College of Engineering Physics, Shenzhen Technology University, Shenzhen 518118, China*

[5]*Hefei National Laboratory, Department of Modern Physics, University of Science and Technology of China, Hefei 230026, China*

(Received 3 December 2023; revised 11 March 2024; accepted 4 April 2024; published 22 April 2024)

We propose a temporal double-slit interferometric scheme to characterize the shaped intense femtosecond laser pulse directly, which can be applied to control electron tunneling wave packets with attosecond precision. By manipulating the spectral phase of the input femtosecond pulse in the frequency domain, one single pulse is split into two subpulses and their waveforms can be controlled by adjusting the spectral phase. In the interaction between the shaped pulse and atoms, the two subpulses are analogous to Young's double slit in the time domain. The interference pattern in the photoelectron momentum distribution can be used to retrieve the peak electric field and the time delay between two subpulses. Based on the characterization of the shaped pulse, we demonstrate that the subcycle dynamics of photoelectrons can be controlled with attosecond precision. The feasibility of this scheme is confirmed through quantum-trajectory Monte Carlo simulations and numerical solutions of the three-dimensional time-dependent Schrödinger equation.

DOI: 10.1103/PhysRevA.109.043115

I. INTRODUCTION

Since the advent of laser technology, precise control over electron motion in atoms and molecules has become possible. Considering the timescale of electron motion, femtosecond or even attosecond lasers are indispensable to modulate electron dynamics [1–4]. One can directly change the parameters of a single laser pulse, such as the carrier-envelope phase [5], wavelength [6], intensity [7], and ellipticity [8]. In addition, one can also construct a pump-probe scheme by varying the time delay between two femtosecond lasers [9–11] or one femtosecond laser plus one attosecond laser [12–17]. Recently, direct combination of two-color laser fields to form a shaped laser field in the temporal domain [18–22], which can be controlled by varying the parameters of the two lasers, has been applied to modulate the motion of tunneling electron wave packets. Moreover, the technology of femtosecond pulse shaping [23,24], which employs Fourier synthesis methods to generate nearly arbitrarily shaped ultrafast optical waveforms with a single laser, has been successfully developed to manipulate the evolution of a quantum system [25,26]. This technique can control various atomic and molecular processes, such as high harmonic generation [27,28] and strong-field ionization of molecules [29,30].

How precise the control of electron dynamics can be achieved depends not only on the ability to subtly alter the laser field, but also on the accuracy with which it can be characterized. Since the electron dynamics is sensitive to the temporal shape of the laser field [19,31], the control of the electron dynamics with attosecond precision requires higher demands for the control and measurement of the laser field in the time domain. Femtosecond pulse shaping is a ideal solution due to its ability to temporally reshape the laser field with great precision and flexibility. However, direct measurement of the tailored laser field remains a challenge, which limits further control of electron motion with high precision. In practice, the shaped laser field is reconstructed based on information of the input laser, which is equally difficult to measure accurately. As a result, the shaped laser field can only be estimated in an uncertain way, far from the requirements. In this work, by introducing the temporal double-slit interferometer, we theoretically propose a scheme to directly measure the shaped laser field. Numerical calculations estimate the error to be within 5%. Based on this, control of the electron tunneling wave packets in attosecond resolution with a shaped femtosecond laser pulse is achieved. Atomic units ($\hbar = m_e = e = 1$) are used throughout the paper unless explicitly stated otherwise.

II. THEORETICAL FRAMEWORK

A. Methods of laser pulse shaping

First, we describe how the shaped pulse is obtained in the experiment. The $4f$ pulse shaping system is a common

*These authors contributed equally to this work.
†xlhao@sxu.edu.cn
‡ccwang@jlu.edu.cn
§chenjing@ustc.edu.cn

method that uses spectral phase modulation to shape the pulse. This method is more accurate than those that control the pulse shape in the time domain. The $4f$ pulse shaper disperses the femtosecond laser pulse spatially onto a spatial light modulator (SLM) using the first grating and lens. In the Fourier plane, the pulse spectrum is split into different frequency components to modulate their corresponding amplitude and phase using the SLM. By applying specific voltages to individual pixels (generally, 1 nm bandwidth can correspond to six pixels) of the SLM, the optical path of each pixel's corresponding wavelength can be independently varied, enabling precise control of the phase change for these wavelengths. Subsequently, the phase-modulated laser pulse propagates through another grating and lens, converting the femtosecond laser pulse from the frequency domain to the time domain (see [32] for details).

In theory, for a linearly polarized laser pulse, the temporal electric field $\boldsymbol{F}(t)$ in the polarized direction (z axis) is

$$\boldsymbol{F}(t) = \tfrac{1}{2}F_0 f(t)e^{i\omega_0 t}\mathbf{e}_z + \text{c.c.}, \tag{1}$$

where F_0 is the amplitude of the electric field, ω_0 is the center frequency (corresponding to wavelength λ_0), and $f(t)$ is the temporal envelope of the electric field that is assumed to be in the Gaussian shape

$$f(t) = e^{-t^2/\Gamma^2}, \tag{2}$$

with Γ defining the full width at half maximum (FWHM) of the laser pulse. The above laser pulse in the frequency domain can be written as

$$f(\omega) = \int_{-\infty}^{+\infty} f(t)e^{-i\omega t}dt \tag{3}$$

by Fourier transformation. By adding a phase π to the frequency spectrum in the frequency range $\omega < \omega_s$, corresponding to the wavelength range $\lambda > \lambda_s$, and applying the inverse Fourier transform, we get

$$\begin{aligned} f_s(\omega_s, t) &= \frac{1}{2\pi}\left(\int_{-\infty}^{\omega_s} f(\omega)e^{i\omega t}e^{i\pi}d\omega + \int_{\omega_s}^{+\infty} f(\omega)e^{i\omega t}d\omega\right) \\ &= |f_s(\omega_s, t)|e^{i\theta(t)}, \end{aligned} \tag{4}$$

where $\theta(t)$ is the temporal phase originated from the introduction of the π phase in the frequency domain. Finally, a shaped electric field depending on ω_s can be rewritten as

$$\begin{aligned} \boldsymbol{F}(\omega_s, t) &= \tfrac{1}{2}F_0|f_s(\omega_s, t)|e^{i[\omega_0 t+\theta(t)]}\mathbf{e}_z + \text{c.c.} \\ &= F_0|f_s(\omega_s, t)|\cos[\omega_0 t + \theta(t)]\mathbf{e}_z, \end{aligned} \tag{5}$$

where $|f_s(\omega_s, t)|$ is the shaped temporal envelope of the electric field.

B. Time-dependent Schrödinger equation calculation

We numerically solve the three-dimensional time-dependent Schrödinger equation (TDSE) within the single-active-electron approximation. In the velocity gauge, the TDSE reads

$$i\frac{\partial}{\partial t}\Psi(\mathbf{r}, t) = \left(-\frac{\nabla^2}{2} + V(\mathbf{r}) - i\mathbf{A}(t)\cdot\boldsymbol{\nabla}\right)\Psi(\mathbf{r}, t), \tag{6}$$

where $\Psi(\mathbf{r}, t)$ is the time-dependent electron wave function and $\mathbf{A}(t) = -\int_{-\infty}^{t}\mathbf{F}(\tau)d\tau$ is the vector potential. We use a parametric model potential

$$V(r) = -(1 + a_1e^{-a_2r} + a_3re^{-a_4r} + a_5e^{-a_6r})/r \tag{7}$$

to represent the electron-core interaction for the Xe atom. In this model potential, the parameters are $a_i = (3.469, 0.684, 50.44, 2.753, 49.53, 5.511)$ $(i = 1, 2, \ldots, 6)$, which are optimized to reproduce as accurately as possible the valence state energies of the Xe atom with $I_p = 0.446$ a.u. (12.13 eV). The initial magnetic quantum number m was tuned to 0.

To solve the TDSE, the split-Lanczos propagator [33,34] is used to propagate the wave function in time, which greatly improves the efficiency of the traditional Lanczos propagator by splitting the centrifugal potential from the Hamiltonian. In our calculations, the wave function is expanded in a product basis with spherical harmonics for the angular part and a finite-element discrete-variable representation [35–37] for the radial part. In addition, we adopt the wave-splitting technique [38] to avoid the use of a very large radial box. The splitting error is controlled by the preset time step dt. According to the wave-splitting technology, at the end time t_f of the propagation, we obtain the final ionization amplitude $f(\mathbf{k}, t_f)$ by adding all the amplitudes at time t_f, where $\mathbf{k}$ is the photoelectron final momentum. Therefore, the differential ionization probability in the x-z plane is $P(\mathbf{k}, \theta) = k|f(k, \theta, \varphi = 0, t_f)|^2$, where θ and φ are the azimuthal and polar angles in spherical coordinates, respectively.

In our TDSE simulation, the FWHM of the laser pulse is 20 fs. The numerical convergence of the calculation has been verified. After a careful check, we find that $L_{\max} = 50$, $R = 2400$ a.u., and $dt = 0.01$ a.u. are sufficient to ensure the convergence for the laser parameters chosen in this work. Note that we choose an even parity of the initial state in the projection to achieve agreement of the angular distribution between the TDSE and quantum trajectory Monte Carlo (QTMC) results.

C. Quantum trajectory Monte Carlo model

In the QTMC model [39,40], the ionization rate is based on the tunneling ionization theory of Ammosov, Delone, and Krainov, i.e., $W(t_i, v_\perp) = W_0(t_i)W_1(v_\perp)$, in which

$$W_0(t_i) = |2(2I_p)^{3/2}/F(t_i)|^{2/\sqrt{2I_p}-1}\exp\left(\frac{-2(2I_p)^{3/2}}{|3F(t_i)|}\right) \tag{8}$$

determines the ionization rate with respect to the tunneling time t_i and

$$W_1(v_\perp) = \frac{1}{\pi}[\sqrt{2I_p}/|F(t_i)|]\exp\left(-\frac{\sqrt{2I_p}(v_\perp)^2}{|F(t_i)|}\right) \tag{9}$$

determines the initial transverse momentum distribution, where I_p is the ionization potential, $v_\perp$ is the initial transverse momentum, and $F(t_i)$ is the instantaneous strength of the laser field. The electron tunneling exit is give by $z(t_i) = -2I_p/F(t_i)/[1 + \sqrt{1 + \gamma^2(t_i)}]$ [40], where $\gamma(t_i) = \sqrt{2I_p}\omega_0/F(t_i)$ is the Keldysh parameter. After ionization, the classical motion of the electron in the combined laser field and

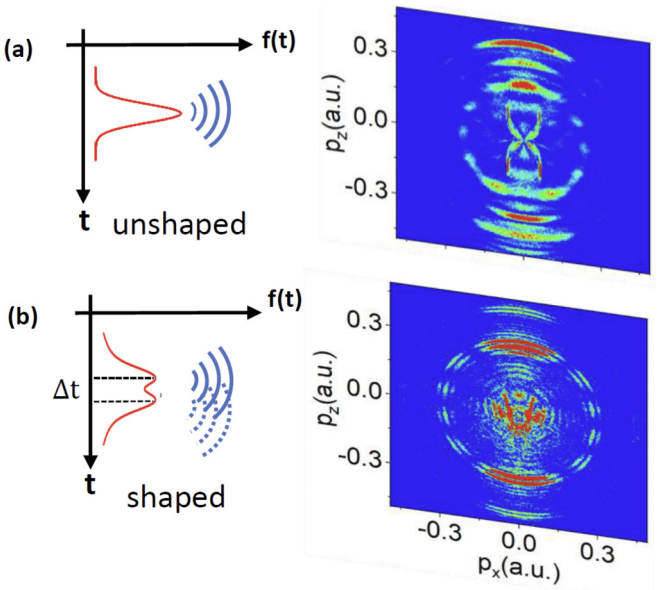

FIG. 1. Sketch of the maps for ionization processes if Xe atoms are exposed to (a) the unshaped single pulse and (b) the shaped pulse with a time delay of Δt between the two subpulses. The PMDs are simulated by the QTMC method. The laser intensity of the input unshaped pulse is $I_0 = 1.5 \times 10^{14}$ W/cm^2, the central wavelength is $\lambda_0 = 800$ nm, and the pulse duration is 20 fs.

Coulomb field is governed by Newton's equation

$$\ddot{\mathbf{r}} = -\nabla V(r) - \mathbf{F}(t), \tag{10}$$

where $V(r)$ is the model potential of the Xe atom [Eq. (7)]. According to the Feynman path-integral approach, the phase is given by the classical action

$$S_j(\mathbf{p}, t_i) = \int_{t_i}^{\infty} [\mathbf{p}^2(\tau)/2 + I_p + V(\mathbf{r})]d\tau, \tag{11}$$

where $\mathbf{p}$ is the instantaneous momentum of the electron. The final distribution is obtained by the coherent sum of different trajectories

$$|\Psi_p|^2 = \left| \sum_j \sqrt{W(t_i, v_\perp^j)} \exp[-iS_j(\mathbf{p}, t_i)] \right|^2. \tag{12}$$

III. RESULTS AND DISCUSSION

As illustrated in Fig. 1, a conventional single femtosecond intense laser pulse can be refashioned into a pair of subpulses by adding a phase of π in the spectra from a specific wavelength λ_s in the frequency domain. The shape of the output pulse, which is mainly determined by the amplitude of the two subpulses and the time delay between them, can be controlled by adjusting λ_s. The shaped laser field corresponding to the specific λ_s is measured base on the principle of Young's double-slit interference in the time domain [41]. The basic idea behind this technique is as follows. If atoms are exposed to a single, intense, unshaped laser pulse, they will be ionized and exhibit a typical photoelectron momentum distribution (PMD) characterized by a series of above-threshold-ionization (ATI) rings separated by one photon energy [6], as shown in Fig. 1(a). Meanwhile, the ATI ring displays stripes at specific angles, known as a jetlike structure. When the shaped pulse is used to ionize atoms, the photoelectrons born in the two subpulses will interfere, resulting in the ATI ring splitting into several subrings [see Fig. 1(b)], while the jetlike structure survives. Similar interpulse interference is theoretically observed in the case of photoionization by an extreme ultraviolet (XUV) laser pulse train combined with an infrared laser field [42], where ionization is produced by the XUV pulse train while the phase of the photoelectron is mainly determined by the infrared pulse. The amplitude and the time delay of the two subpulses can be retrieved by analyzing the positions and fringe spacing of the subrings, just like what is done in Young's double-slit experiment for light. We call this technique Young's temporal double-slit interferometry. Then, by varying λ_s, very subtle changes of the shape of the tailored pulse can be characterized. With this capability, we can manipulate the electron tunneling dynamics with attosecond precision. Note that the temporal double-slit interference in strong-field tunneling ionization was first observed in few-cycle laser pulses [41]. At a particular carrier-envelope phase, ionization occurs for two dominant durations in two adjacent optical cycles, on either side of the maximum of the laser envelope. These durations are treated as two slits in the time domain and produce interference fringes in the photoelectron spectrum. In this work, there are also two durations of ionization at the two subpulses, which are treated as two temporal slits but with a much greater time delay. Additionally, the time delay between the two slits in the shaped pulse can be conveniently regulated, but that of the few-cycle laser pulse is constant, approximately equal to the optical cycle.

First, we will demonstrate that the subring structure in Fig. 1(b) is the result of interference between ionization events from different subpulses. In simulations of the QTMC method, we can explicitly obtain the PMDs corresponding to ionization events born in a selected range of time in the shaped pulse. If the ionization is confined to a single subpulse, for example, $t_i < 0$ in Fig. 2(ai), the PMD shows features similar to the case of the unshaped pulse: Clear ATI rings without splitting are modulated with a jetlike structure, as shown within the white dashed lines in Fig. 2(b). The ATI rings with a spacing of one photon energy are usually recognized as the result of interference between electrons ionized in adjacent optical cycles, which is known as intercycle interference [43]. The jetlike structure can be attributed to the intracycle interference of electrons ionized in an optical cycle [39], also known as intracycle interference [41]. As shown in Fig. 2(aii), electrons emitted at times t_{i1} and t_{i2} possess an identical final momentum of $\mathbf{p} = -\mathbf{A}(t_i)$ within the strong-field approximation (SFA) [44], where $\mathbf{A}(t_i)$ is the vector potential. Subsequently, these electrons will interfere, which can be demonstrated explicitly by considering electrons ionized within only one optical cycle [the region in the dashed box in Fig. 2(ai)], as shown in Fig. 2(c). In this case, intracycle interference causes the jetlike structure prevalence in the PMD.

Figure 2(b) suggests that ionizations in both subpulses are necessary for the formation of the subring structure. If the ionization times are limited to two symmetric half optical cycles in the negative direction around the envelope maximum

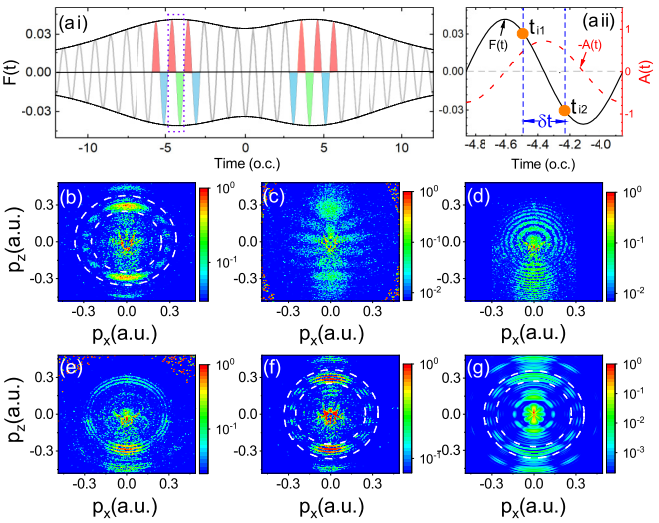

FIG. 2. (ai) Electric field $F(t)$ of the shaped pulse as a function of time. (aii) Electric field and negative vector potential $-A(t)$ within one optical cycle indicated by the violet dashed rectangle shown in (ai). Here t_{i1} and t_{i2} denote the ionization times of intracycle interference trajectories which have the same final momentum with a time difference δt. Simulated PMDs by QTMC are obtained by considering electrons ionized at different time ranges: (b) $t_i < 0$, (c) t_i in a single optical cycle enclosed by the dashed rectangle, (d) t_i in green regions, (e) t_i in green and blue regions, and (f) t_i in green, blue, and red regions. (g) The PMD calculated by the TDSE. The white dashed lines are used to indicate the subring and jetlike structure. Here $\lambda_s = 780$ nm and the other pulse parameters are the same as in Fig. 1.

of each subpulse [green regions in Fig. 2(ai)], the interference of electrons ionized in these regions generates a multitude of rings, as shown in Fig. 2(d). The spacing of these rings corresponds to that of the subring structure in Fig. 1(b). Further, when electrons originating from adjacent half optical cycles in the negative-field direction [blue regions in Fig. 2(ai)] are also involved, adjacent intercycle interference comes into play and the subring structure is modulated by ATI rings, as shown in Fig. 2(e). Finally, by adding electrons ionized in the positive electric field [red regions in Fig. 2(ai)], intracycle interference results in the formation of the jetlike structure [within white dashed lines in Fig. 2(f)]. This almost entirely reproduces the complete PMDs for the shaped pulse in Fig. 1(b). Therefore, it can be concluded that the subring structure in the PMDs of the shaped pulse is the result of interference between the electrons ionized in the two subpulses, which constitutes double-slit interference in the time domain. Additionally, in Fig. 2(g) we also present simulated PMDs by numerically solving the three-dimensional TDSE. The same laser parameters that were utilized in the QTMC calculations are applied. The TDSE-simulated PMD, which also features the split ATI rings along with a jetlike structure [within the white dashed lines in Fig. 2(g)], exhibits excellent agreement with the QTMC results presented in Figs. 2(f) and 1(b).

Based on the principle of Young's double-slit interference, the interference fringes in the PMDs are used to retrieve the peak field and time delay of the shaped pulse consisting of two subpulses. The interference fringe spacing is closely related to the time delay between the two subpulses. The relation can be obtained based on the SFA [44], in which the Coulomb field between the ionized electron and the residual core is neglected. For an electron ionized at t_i with final momentum $\mathbf{p}$, the classical action can be written as

$$S(\mathbf{p}, t_i) = \int_{t_i}^{\infty} dt \left\{ \frac{1}{2}[\mathbf{p} + \mathbf{A}(t)]^2 + I_p \right\}. \tag{13}$$

The phase difference ΔS between two trajectories ionized at t_{i2} and t_{i1} can be expressed as

$$\begin{aligned} \Delta S &= S(t_{i1}) - S(t_{i2}) \\ &= (E + I_p + U_p)\Delta t + \frac{p_z A_0}{\omega_0}[\cos(\omega_0 t_{i2}) - \cos(\omega_0 t_{i1})] \\ &\quad - \frac{U_p}{2\omega_0}[\sin(2\omega_0 t_{i2}) - \sin(2\omega_0 t_{i1})], \end{aligned} \tag{14}$$

where $\Delta t = t_{i2} - t_{i1}$ and $E = p^2/2$. Here the vector potential $\mathbf{A}(t)$ is approximated as $\mathbf{A}(t) = -A_0 \sin(w_0 t)\mathbf{e}_z$ for the sake of simplification and $U_p = F_0^2/4\omega_0^2$ is the ponderomotive energy.

For interference between electrons ionized at the two subpulses, t_{i1} and t_{i2} are at the two envelope peaks of the shaped pulse and Δt is equal to the time delay between the two subpulses. If the time zero is chosen at the middle of the shaped pulse, we have $t_{i1} + t_{i2} = 0$ due to the symmetry of the two subpulses. Then the phase difference in Eq. (14) can be obtained as

$$\Delta S = (E + I_p + U_p)\Delta t - \frac{U_p}{\omega_0}\sin(\omega_0 \Delta t) = 2m\pi. \tag{15}$$

When the electron varies ΔE, which is just equal to the fringe spacing of the subrings in the PMD, the phase difference changes 2π. Then the time delay Δt can be extracted as

$$\Delta t = 2\pi/\Delta E. \tag{16}$$

Therefore, we only have to read the fringe spacing in the PMD to obtain the time delay.

Further, once the exact value of m in Eq. (15) is known, we can determine U_p and thus determine the peak electric field F_0 of the shaped pulse. This can be achieved with the help of the jetlike structure of the PMDs. The jetlike structure has been widely discussed previously and can be explained by either multiphoton ionization [45,46] or subcycle electron wave-packet interference [47]. The number of nodes in the jetlike structure on the ATI ring is closely related to the number of absorbed photons [48]. In the case of ten nodes in Fig. 1(b), this corresponds to an 11-photon channel. We can deduce a guessed U_p according to the energy conservation, i.e., $n\omega_0 - I_p - U_p = E$, which describes that a bounded electron absorbs n photons to overcome the binding potential I_p plus the ponderomotive potential U_p and eventually becomes a free electron with energy E. Then we substitute the guessed U_p into Eq. (15) to make a correction to it by ensuring that m is an integer. Eventually, both the peak electric field and the time delay of the two subpulses are obtained for a specific λ_s. Varying λ_s will cause the shape of the tailored laser field to change, resulting in the shift of interference fringes and alteration of the fringe spacing. This can be seen clearly in the angle-integrated energy spectra simulated by both QTMC

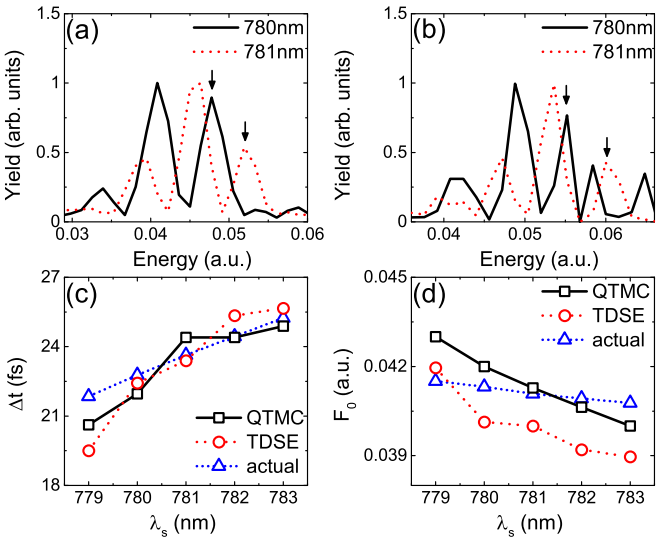

FIG. 3. Energy spectra for shaped pulses simulated by the (a) QTMC and (b) TDSE methods and the corresponding (c) extracted time delay Δt and (d) peak-electric-field strength F_0 of the shaped pulse at different λ_s. The actual values of Δt and F_0 are also presented for comparison. The arrows in (a) and (b) are used to indicate the subring used in Fig. 4.

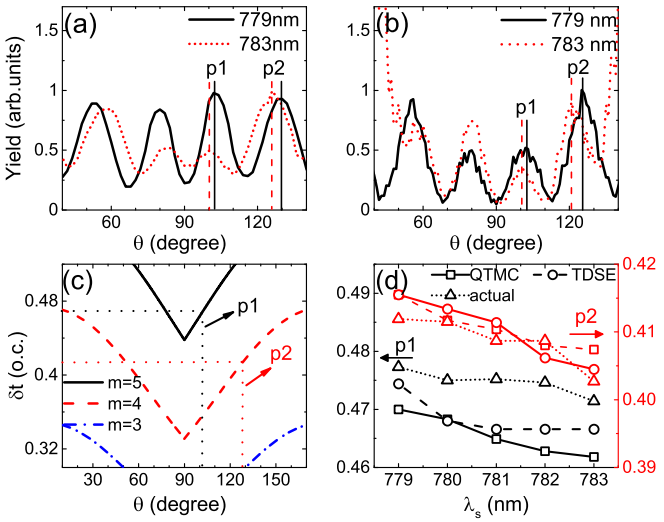

FIG. 4. Angular distribution corresponding to a specific subring at different λ_s simulated by the (a) QTMC and (b) TDSE methods. The positions for peaks p1 and p2 are indicated by vertical lines. (c) Curves obtained from Eq. (18), illustrating how the ionization time difference δt between the two interfering electron trajectories contributing to the two peaks (labeled p1 and p2) in (a) and (b) can be extracted from the curves. (d) Extracted λ_s-dependent δt corresponding to peaks p1 and p2. The actual values of δt obtained through the statistics of the trajectories in the QTMC simulations are also presented for comparison. The subrings used above are indicated by arrows in Figs. 3(a) and 3(b).

[Fig. 3(a)] and TDSE [Fig. 3(b)] methods, in which the peaks shift to the right and the spacing between them decreases when λ_s increases. Applying Young's temporal double-slit interferometry, Δt and F_0 for different λ_s are extracted from the simulated photoelectron spectra, as shown in Figs. 3(c) and 3(d). For comparison, we also present the actual values read directly from the shaped pulse. The results retrieved for both QTMC and TDSE methods are found to be in good agreement with the actual values within 5% error, which proves the accuracy of the interferometer. From Figs. 3(c) and 3(d) it can be observed that the time delay and peak electric field vary almost linearly with λ_s. Therefore, by obtaining the slope of the λ_s dependence in experiments using only a few data points, we can directly read the time delay and peak intensity for other λ_s from the curve without having to measure them with the help of the PMD. For example, the slope of the time delay versus λ_s in Fig. 3(c) is approximately 1097 as/nm; then the corresponding step of the time delay for the shortest step of adjusting λ_s that can be achieved, i.e., 0.2 nm, would be 220 as. It is worth noting that there is a larger deviation of the TDSE reconstructed values of F_0 from the actual values compared to the QTMC results. This deviation can be attributed to the averaging effect of the laser electric field. The final PMD is the sum of contributions from electrons ionized at different laser fields with varying probabilities. Thus, the F_0 extracted from the PMD represents an average laser field that is lower than the peak electric field. The QTMC calculations employ the Ammosov-Delone-Krainov formula to determine the field-dependent ionization rate, which is highly sensitive to the laser field. The spectra are primarily influenced by ionization at the peak electric field, resulting in the extracted value of F_0 being closer to the peak electric field even after averaging the laser electric field. In contrast, the ionization rate in TDSE calculations is less sensitive to the laser electric field, making the averaging effect more prominent. This is supported by the shift of the energy peaks in the spectra in Fig. 3(b) simulated by the TDSE method compared to that in Fig. 3(a) obtained by the QTMC method. As a result, the TDSE extracted F_0 differs more from the actual values of the peak laser electric field compared to the QTMC results.

The precise control of electronic dynamics becomes possible after accurately characterizing the electric-field waveform of the shaped pulse. The λ_s-dependent subring structure in the PMDs has demonstrated the ability of the shaped pulse to control the dynamics of tunneling wave packets. However, this kind of manipulation of electron motion is limited to half the optical cycle (1.3 fs for the 800-nm laser pulse), since the subring structure is the result of the intercycle interference, although the precision of modulating the time delay between the two subpulses can be achieved on the attosecond scale. In fact, along with the ability to control the time delay of the shaped pulse, we can also precisely modulate its peak-electric-field strength concurrently [see Fig. 3(d)]. Here we exploit the latter capability to control the electron subcycle dynamics with attosecond precision. For this purpose, we investigate the photoelectron angular distribution featured with a series of peaks, corresponding to the jetlike structure in the PMDs, which is sensitive to the peak electric field. Examining the jetlike structure for a specific subring, we find that the peaks in the photoelectron angular distribution simulated by both the TDSE and QTMC methods shrink towards 90° (perpendicular to the laser polarization) with increasing λ_s, as shown in Figs. 4(a) and 4(b). Since the jetlike structure is the result of the intracycle interference,

its evolution with λ_s indicates the possibility of manipulating the electron dynamics with subcycle precision. This subcycle dynamics is characterized by δt, the difference in ionization time for the two interfering electron trajectories born within an optical cycle, as sketched in Fig. 2(aii), which can be extracted from the angular distribution by phase analysis. In the case of intracycle interference leading to the jetlike structure, the two interfering trajectories ionized at different times t_{i1} and t_{i2} in an optical cycle but with the same final longitudinal momentum p_z satisfy the condition $\omega_0(t_{i1}+t_{i2})=(2k+1)\pi$, where k is even for $p_z>0$ and odd for $p_z<0$. So the phase difference in Eq. (14) can be rewritten as

$$\Delta S=(E+I_p+U_p)\delta t-\frac{2\sqrt{2E}F_0}{\omega_0^2}|\cos\theta|\sin\left(\frac{\omega_0}{2}\delta t\right)-\frac{U_p}{\omega_0}\sin(\omega_0\delta t), \tag{17}$$

where $\delta t=t_{i2}-t_{i1}$ is the ionization time delay between the two trajectories and θ is the angle between the photoelectron's emission direction and the laser polarization. The peak at a specific angle θ in the angular distribution occurs when the phase difference between the two trajectories experiencing the intracycle interference reaches $2m\pi$, which gives the relationship

$$(E+I_p+U_p)\delta t-\frac{2\sqrt{2E}F_0}{\omega_0^2}|\cos\theta|\sin\left(\frac{\omega_0}{2}\delta t\right)-\frac{U_p}{\omega_0}\sin(\omega_0\delta t)=2m\pi. \tag{18}$$

Given the photoelectron energy E and peak-electric-field strength F_0, a specific relationship between δt and θ for certain m values can be established using the mean values of E and F_0 at different λ_s. This relationship can be determined through the curves provided by Eq. (18), which are illustrated in Fig. 4(c). According to the phase analysis, if one counts the number of peaks in the angular distribution starting from 90°, the first peak corresponds to the largest m allowed by Eq. (18), the second peak corresponds to $m-1$, and so on. Therefore, δt for peak p1 in Fig. 4(a) should be extracted from the curve of $m=5$ and δt for peak p2 should be read from the curve of $m=4$, as illustrated in Fig. 4(c). In Fig. 4(d) we present the δt extracted from spectra simulated by the QTMC and TDSE methods at different λ_s, which exhibits a decreasing trend in the dependence on λ_s. We also provide the actual values of δt obtained through the statistics of the trajectories contributing to the peaks in the QTMC simulations. The good agreement between the extracted δt for both the QTMC and TDSE methods with the actual values supports the validity of the extraction method. The results in Fig. 4(d) clearly demonstrate that the subcycle electronic dynamics, characterized by δt, can be manipulated with attosecond precision by regulating the shaped laser field. The slopes of the curve for δt extracted from peaks p1 and p2 are approximately 4 and 7 as/nm, respectively. Note that there is a greater discrepancy between the extracted and actual values for peak p1 compared to peak p2. There are three types of electron trajectories involved in the formation of p1 and p2 when the Coulomb field is included [39]. The first type is direct electrons and the second type is indirect electrons with a large initial transverse velocity. The latter can return to the parent ion's coordinate in the direction of laser polarization, but with a significant perpendicular distance due to the electrons' large initial transverse velocity. They will only experience a slight deflection from a ballistic trajectory. The third type refers to rescattering electrons with a small initial transverse velocity, which return to collide with the parent ion and experience a stronger influence from the parent ion. Peak p1 comes from the interference between all three types of trajectories, while peak p2 is only due to the interference between the direct and indirect trajectories. If the Coulomb effect is not taken into account, both peaks are formed by the constructive interference between the direct and indirect electrons. In Eq. (18) we do not consider the Coulomb effect or the contribution of rescattering electrons in our extraction process. Therefore, the difference between the extracted and actual values for peak p1 is larger than that for p2.

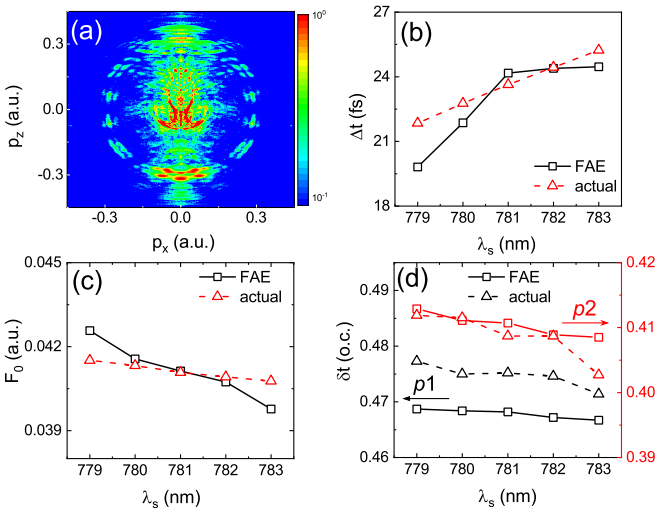

FIG. 5. (a) PMD calculated by the QTMC method including the focal-volume-averaging effect (FAE), where $\lambda_s=780$ nm and the peak laser intensity is 1.5×10^{14} W/cm^2. The corresponding λ_s dependences of (b) the extracted time delay Δt, (c) the peak-electric-field strength F_0 of the shaped pulse, and (d) δt corresponding to peaks p1 and p2 are compared with the actual values.

Finally, to demonstrate the applicability of our scheme in the actual experiments, we apply focal-volume averaging to the numerical calculations of the QTMC method, as shown in Fig. 5. The subring structure in PMDs still persists after focal-volume averaging, and the jetlike structure agrees well with the results presented in Fig. 1(b). Based on the focal-volume-averaged PMD, we can employ the aforementioned workflow to extract the time delay Δt [Fig. 5(b)], the peak-electric-field strength F_0 [Fig. 5(c)] of the shaped pulse, and δt corresponding to peaks p1 and p2 [Fig. 5(d)]. The agreement of the extracted results and the actual values in Figs. 5(b)–5(d) supports the reliability of our retrieval methods in the real experiments.

IV. CONCLUSION

In summary, we have proposed a Young temporal double-slit interferometer to characterize the shaped laser field. By reversing the phase of the frequency spectra from a specific wavelength λ_s, a conventional single femtosecond pulse is split into a pair of subpulses in the time domain after the Fourier transform, whose shape can be precisely controlled by adjusting λ_s. Based on the principle of Young's double-slit interference in the time domain, in which the two subpulses are analogous to the double slit, the peak electric field and the time delay between them can be retrieved from the interference pattern in PMDs to within 5% error. With this capability, we showed that the subcycle dynamics of the electron can be controlled with shaped pulses and the precision of the control is in the attosecond scale. The above scheme was proved to be feasible by both QTMC and TDSE simulations.

In real experiments, it is necessary to consider unavoidable experimental errors, but they have little effect on the precision of this method. The pulse shaper introduces experimental errors to the phase change, which have two aspects. First, the properties of the liquid crystal of the SLM vary with temperature. After stabilizing the temperature of the SLM, the error in phase modulation is typically less than 0.3%. Second, the error in voltage modulation of the phase is less than 0.2%. These minor phase errors have minimal impact on the temporal shape of the laser pulse. Additionally, varying the intensity of the initial laser pulse may induce energy shifts in the spectra, potentially affecting the precision of this method. However, the fluctuation of the initial pulse from pulse to pulse is less than 1%, which corresponds to errors below 1% in the energy spectra. Therefore, the impact on precision is minimal. It is worth noting that the shaped pulse consisting of two subpulses can also be regarded as the construction of a pump-probe scheme. Our work demonstrated that the time delay between the pump and probe pulses can be manipulated with attosecond precision. In addition, the proposed scheme can also be extended to circularly polarized laser fields to be combined with attoclock technology, which may be capable of probing and controlling electronic dynamics with even higher precision.

ACKNOWLEDGMENTS

This work was supported by the National Key Research and Development Program (Grant No. 2019YFA0307700), the National Natural Science Foundation of China (Grants No. 12274273, No. 12204314, No. 92261201, and No. 12274179), the Innovation Program for Quantum Science and Technology (Grant No. 2021ZD0302101), and the Natural and Science Foundation of Top Talent of SZTU (Grant No. GDRC202202).

[1] H. Niikura, F. Légaré, R. Hasbani, A. D. Bandrauk, M. Y. Ivanov, D. M. Villeneuve, and P. B. Corkum, Sublaser-cycle electron pulses for probing molecular dynamics, Nature (London) **417**, 917 (2002).

[2] E. Goulielmakis, Z.-H. Loh, A. Wirth, R. Santra, N. Rohringer, V. S. Yakovlev, S. Zherebtsov, T. Pfeifer, A. M. Azzeer, M. F. Kling, S. R. Leone, and F. Krausz, Real-time observation of valence electron motion, Nature (London) **466**, 739 (2010).

[3] A. Baltuška, T. Udem, M. Uiberacker, M. Hentschel, E. Goulielmakis, C. Gohle, R. Holzwarth, V. S. Yakovlev, A. Scrinzi, T. W. Hänsch, and F. Krausz, Attosecond control of electronic processes by intense light fields, Nature (London) **421**, 611 (2003).

[4] S. R. Leone, C. W. McCurdy, J. Burgdörfer, L. S. Cederbaum, Z. Chang, N. Dudovich, J. Feist, C. H. Greene, M. Ivanov, R. Kienberger, U. Keller, M. F. Kling, Z.-H. Loh, T. Pfeifer, A. N. Pfeiffer, R. Santra, K. Schafer, A. Stolow, U. Thumm, and M. J. J. Vrakking, What will it take to observe processes in 'real time'? Nat. Photon. **8**, 162 (2014).

[5] G. G. Paulus, F. Lindner, H. Walther, A. Baltuška, E. Goulielmakis, M. Lezius, and F. Krausz, Measurement of the phase of few-cycle laser pulses, Phys. Rev. Lett. **91**, 253004 (2003).

[6] C. M. Maharjan, A. S. Alnaser, I. Litvinyuk, P. Ranitovic, and C. L. Cocke, Wavelength dependence of momentum-space images of low-energy electrons generated by short intense laser pulses at high intensities, J. Phys. B **39**, 1955 (2006).

[7] B. Walker, B. Sheehy, L. F. DiMauro, P. Agostini, K. J. Schafer, and K. C. Kulander, Precision measurement of strong field double ionization of helium, Phys. Rev. Lett. **73**, 1227 (1994).

[8] H. Kang, K. Henrichs, M. Kunitski, Y. Wang, X. Hao, K. Fehre, A. Czasch, S. Eckart, L. Schmidt, M. Schöffler, T. Jahnke, X. Liu, and R. Dörner, Timing recollision in nonsequential double ionization by intense elliptically polarized laser pulses, Phys. Rev. Lett. **120**, 223204 (2018).

[9] A. H. Zewail, Laser femtochemistry, Science **242**, 1645 (1988).

[10] A. H. Zewail, Femtochemistry: Atomic-scale dynamics of the chemical bond, J. Phys. Chem. A **104**, 5660 (2000).

[11] M. Dantus, R. M. Bowman, and A. H. Zewail, Femtosecond laser observations of molecular vibration and rotation, Nature (London) **343**, 737 (1990).

[12] D. Huh, B. D. Matthews, A. Mammoto, M. Montoya-Zavala, H. Y. Hsin, and D. E. Ingber, Reconstituting organ-level lung functions on a chip, Science **328**, 1662 (2010).

[13] A. L. Cavalieri, N. Müller, T. Uphues, V. S. Yakovlev, A. Baltuška, B. Horvath, B. Schmidt, L. Blümel, R. Holzwarth, S. Hendel, M. Drescher, U. Kleineberg, P. M. Echenique, R. Kienberger, F. Krausz, and U. Heinzmann, Attosecond spectroscopy in condensed matter, Nature (London) **449**, 1029 (2007).

[14] K. Klünder, J. M. Dahlström, M. Gisselbrecht, T. Fordell, M. Swoboda, D. Guénot, P. Johnsson, J. Caillat, J. Mauritsson, A. Maquet, R. Taïeb, and A. L'Huillier, Probing single-photon ionization on the attosecond time scale, Phys. Rev. Lett. **106**, 143002 (2011).

[15] M. Ossiander, F. Siegrist, V. Shirvanyan, R. Pazourek, A. Sommer, T. Latka, A. Guggenmos, S. Nagele, J. Feist, J. Burgdörfer, R. Kienberger, and M. Schultze, Attosecond correlation dynamics, Nat. Phys. **13**, 280 (2017).

[16] M. Swoboda, T. Fordell, K. Klünder, J. M. Dahlström, M. Miranda, C. Buth, K. J. Schafer, J. Mauritsson, A. L'Huillier, and M. Gisselbrecht, Phase measurement of resonant two-photon ionization in helium, Phys. Rev. Lett. **104**, 103003 (2010).

[17] X. Gong, W. Jiang, J. Tong, J. Qiang, P. Lu, H. Ni, R. Lucchese, K. Ueda, and J. Wu, Asymmetric attosecond photoionization in molecular shape resonance, Phys. Rev. X **12**, 011002 (2022).

[18] C. A. Mancuso, D. D. Hickstein, P. Grychtol, R. Knut, O. Kfir, X.-M. Tong, F. Dollar, D. Zusin, M. Gopalakrishnan, C. Gentry, E. Turgut, J. L. Ellis, M.-C. Chen, A. Fleischer, O. Cohen, H. C. Kapteyn, and M. M. Murnane, Strong-field ionization with two-color circularly polarized laser fields, Phys. Rev. A **91**, 031402(R) (2015).

[19] K. Lin, X. Jia, Z. Yu, F. He, J. Ma, H. Li, X. Gong, Q. Song, Q. Ji, W. Zhang, H. Li, P. Lu, H. Zeng, J. Chen, and J. Wu, Comparison study of strong-field ionization of molecules and atoms by bicircular two-color femtosecond laser pulses, Phys. Rev. Lett. **119**, 203202 (2017).

[20] S. Eckart, M. Kunitski, I. Ivanov, M. Richter, K. Fehre, A. Hartung, J. Rist, K. Henrichs, D. Trabert, N. Schlott, L. P. H. Schmidt, T. Jahnke, M. S. Schöffler, A. Kheifets, and R. Dörner, Subcycle interference upon tunnel ionization by counter-rotating two-color fields, Phys. Rev. A **97**, 041402(R) (2018).

[21] M. Han, P. Ge, M.-M. Liu, Q. Gong, and Y. Liu, Spatially and temporally controlling electron spin polarization in strong-field ionization using orthogonal two-color laser fields, Phys. Rev. A **99**, 023404 (2019).

[22] D. B. Milošević, W. Becker, and R. Kopold, Generation of circularly polarized high-order harmonics by two-color coplanar field mixing, Phys. Rev. A **61**, 063403 (2000).

[23] A. M. Weiner, Femtosecond optical pulse shaping and processing, Prog. Quantum Electron. **19**, 161 (1995).

[24] A. M. Weiner, Femtosecond pulse shaping using spatial light modulators, Rev. Sci. Instrum. **71**, 1929 (2000).

[25] T. Brixner, G. Krampert, T. Pfeifer, R. Selle, G. Gerber, M. Wollenhaupt, O. Graefe, C. Horn, D. Liese, and T. Baumert, Quantum control by ultrafast polarization shaping, Phys. Rev. Lett. **92**, 208301 (2004).

[26] N. Dudovich, D. Oron, and Y. Silberberg, Quantum control of the angular momentum distribution in multiphoton absorption processes, Phys. Rev. Lett. **92**, 103003 (2004).

[27] R. Bartels, S. Backus, E. Zeek, L. Misoguti, G. Vdovin, I. P. Christov, M. M. Murnane, and H. C. Kapteyn, Shaped-pulse optimization of coherent emission of high-harmonic soft x-rays, Nature (London) **406**, 164 (2000).

[28] D. Oron, Y. Silberberg, N. Dudovich, and D. M. Villeneuve, Efficient polarization gating of high-order harmonic generation by polarization-shaped ultrashort pulses, Phys. Rev. A **72**, 063816 (2005).

[29] V. Tagliamonti, B. Kaufman, A. Zhao, T. Rozgonyi, P. Marquetand, and T. Weinacht, Time-resolved measurement of internal conversion dynamics in strong-field molecular ionization, Phys. Rev. A **96**, 021401(R) (2017).

[30] B. Kaufman, T. Rozgonyi, P. Marquetand, and T. Weinacht, Coherent control of internal conversion in strong-field molecular ionization, Phys. Rev. Lett. **125**, 053202 (2020).

[31] I. J. Sola, E. Mével, L. Elouga, E. Constant, V. Strelkov, L. Poletto, P. Villoresi, E. Benedetti, J.-P. Caumes, S. Stagira, C. Vozzi, G. Sansone, and M. Nisoli, Controlling attosecond electron dynamics by phase-stabilized polarization gating, Nat. Phys. **2**, 319 (2006).

[32] A. M. Weiner, Ultrafast optical pulse shaping: A tutorial review, Opt. Commun. **284**, 3669 (2011)

[33] W.-C. Jiang and X.-Q. Tian, Efficient split-Lanczos propagator for strong-field ionization of atoms, Opt. Express **25**, 26832 (2017).

[34] M. Liu, X.-Q. Wang, L. Jia, P.-G. Yan, and W.-C. Jiang, Signatures beyond the rotating-wave approximation in retrieving the photoionization time delay from an ω-2ω interferometric method, Phys. Rev. A **108**, 013102 (2023).

[35] T. N. Rescigno and C. W. McCurdy, Numerical grid methods for quantum-mechanical scattering problems, Phys. Rev. A **62**, 032706 (2000).

[36] M. J. Rayson, Lagrange-Lobatto interpolating polynomials in the discrete variable representation, Phys. Rev. E **76**, 026704 (2007).

[37] B. I. Schneider and L. A. Collins, The discrete variable method for the solution of the time-dependent Schrödinger equation, J. Non-Cryst. Solids **351**, 1551 (2005).

[38] X. M. Tong, K. Hino, and N. Toshima, Phase-dependent atomic ionization in few-cycle intense laser fields, Phys. Rev. A **74**, 031405(R) (2006).

[39] M. Li, J.-W. Geng, H. Liu, Y. Deng, C. Wu, L.-Y. Peng, Q. Gong, and Y. Liu, Classical-quantum correspondence for above-threshold ionization, Phys. Rev. Lett. **112**, 113002 (2014).

[40] X. Song, C. Lin, Z. Sheng, P. Liu, Z. Chen, W. Yang, S. Hu, C. D. Lin, and J. Chen, Unraveling nonadiabatic ionization and Coulomb potential effect in strong-field photoelectron holography, Sci. Rep. **6**, 28392 (2016).

[41] F. Lindner, M. G. Schätzel, H. Walther, A. Baltuška, E. Goulielmakis, F. Krausz, D. B. Milošević, D. Bauer, W. Becker, and G. G. Paulus, Attosecond double-slit experiment, Phys. Rev. Lett. **95**, 040401 (2005).

[42] R. Della Picca, M. F. Ciappina, M. Lewenstein, and D. G. Arbó, Laser-assisted photoionization: Streaking, sideband, and pulse-train cases, Phys. Rev. A **102**, 043106 (2020).

[43] D. G. Arbó, K. L. Ishikawa, K. Schiessl, E. Persson, and J. Burgdörfer, Intracycle and intercycle interferences in above-threshold ionization: The time grating, Phys. Rev. A **81**, 021403(R) (2010).

[44] K. Amini, J. Biegert, F. Calegari, A. Chacón, M. F. Ciappina, A. Dauphin, D. K. Efimov, C. F. de Morisson Faria, K. Giergiel, P. Gniewek, A. S. Landsman, M. Lesiuk, M. Mandrysz, A. S. Maxwell, R. Moszyński, L. Ortmann, J. A. Pérez-Hernández, A. Picón, E. Pisanty, J. Prauzner-Bechcicki *et al.*, Symphony on strong field approximation, Rep. Prog. Phys. **82**, 116001 (2019).

[45] V. Schyja, T. Lang, and H. Helm, Channel switching in above-threshold ionization of xenon, Phys. Rev. A **57**, 3692 (1998).

[46] M. Li, P. Zhang, S. Luo, Y. Zhou, Q. Zhang, P. Lan, and P. Lu, Selective enhancement of resonant multiphoton ionization with strong laser fields, Phys. Rev. A **92**, 063404 (2015).

[47] Y. Huismans, A. Rouzée, A. Gijsbertsen, P. S. W. M. Logman, F. Lépine, C. Cauchy, S. Zamith, A. S. Stodolna, J. H. Jungmann,

J. M. Bakker, G. Berden, B. Redlich, A. F. G. van der Meer, K. J. Schafer, and M. J. J. Vrakking, Photoelectron angular distributions from the ionization of xenon Rydberg states by midinfrared radiation, Phys. Rev. A **87**, 033413 (2013).

[48] L. Bai, J. Zhang, Z. Xu, and D.-S. Guo, Photoelectron angular distributions from above threshold ionization of hydrogen atoms in strong laser fields, Phys. Rev. Lett. **97**, 193002 (2006).